

Published in final edited form as:

Neuroimage. 2013 January 1; 64: 640–649. doi:10.1016/j.neuroimage.2012.08.047.

Quantitative magnetization transfer imaging of human brain at 7 T★

Richard D. Dortch^{a,b,*}, Jay Moore^{a,b}, Ke Li^{a,b}, Marcin Jankiewicz^{a,b}, Daniel F. Gochberg^{a,b,c}, Jane A. Hirtle^b, John C. Gore^{a,b,c,d,e}, and Seth A. Smith^{a,b,d}

^aDepartment of Radiology and Radiological Sciences, Vanderbilt University, Nashville, TN, USA

^bVanderbilt University Institute of Imaging Science, Vanderbilt University, Nashville, TN, USA

^cDepartment of Physics and Astronomy, Vanderbilt University, Nashville, TN, USA

^dDepartment of Biomedical Engineering, Vanderbilt University, Nashville, TN, USA

^eDepartment of Molecular Physiology and Biophysics, Vanderbilt University, Nashville, TN, USA

Abstract

Quantitative magnetization transfer (qMT) imaging yields indices describing the interactions between free water protons and immobile macromolecular protons. These indices include the macromolecular to free pool size ratio (*PSR*), which has been shown to be correlated with myelin content in white matter. Because of the long scan times required for whole-brain imaging ($\approx 20\text{--}30$ min), qMT studies of the human brain have not found widespread application. Herein, we investigated whether the increased signal-to-noise ratio available at 7.0 T could be used to reduce qMT scan times. More specifically, we developed a selective inversion recovery (SIR) qMT imaging protocol with a *i*) novel transmit radiofrequency (B_1^+) and static field (B_0) insensitive inversion pulse, *ii*) turbo field-echo readout, and *iii*) reduced TR. In vivo qMT data were obtained in the brains of healthy volunteers at 7.0 T using the resulting protocol (scan time ≈ 40 s/slice, resolution = $2 \times 2 \times 3$ mm³). Reliability was also assessed in repeated acquisitions. The results of this study demonstrate that SIR qMT imaging can be reliably performed within the radiofrequency power restrictions present at 7.0 T, even in the presence of large B_1^+ and B_0 inhomogeneities. Consistent with qMT studies at lower field strengths, the observed *PSR* values were higher in white matter (mean \pm SD = $17.6 \pm 1.3\%$) relative to gray matter ($10.3 \pm 1.6\%$) at 7.0 T. In addition, regional variations in *PSR* were observed in white matter. Together, these results suggest that qMT measurements are feasible at 7.0 T and may eventually allow for the high-resolution assessment of changes in composition throughout the normal and diseased human brain in vivo.

Keywords

Magnetization transfer; 7 T; White matter; Myelin; Brain; Multiple sclerosis

★Grant sponsors: NIH K01 EB009120 (SAS), NIH T32 EB001628 (JCG), NIH EB00461 (JCG), and Vanderbilt Bridge Funding (DFG).

© 2012 Elsevier Inc. All rights reserved.

*Corresponding author at: Vanderbilt University Institute of Imaging Science, AA-1101 Medical Center North, 1161 21st Avenue South, Nashville, TN 37232-2310, USA. Fax: +1 615 322 0734. richard.dortch@vanderbilt.edu. .

Introduction

In addition to the free water protons typically observed in magnetic resonance imaging (MRI), there are protons residing on immobile macromolecules in tissue (Wolff and Balaban, 1989). Typical imaging sequences do not directly detect this pool of protons because they exhibit very short transverse relaxation times ($\approx 10 \mu\text{s}$) and, therefore, lose coherence before their signal can be captured. This macromolecule proton pool can, however, be indirectly detected by exploiting its interactions with the free water pool via chemical exchange and/or dipolar mechanisms [referred to together as the magnetization transfer (MT) effect]. Previous phantom studies (Koenig, 1991; Kucharczyk et al., 1994) have shown that the bulk of the MT effect in white matter (WM) arises from myelin-associated lipids, which suggests that MT contrast may be a more specific marker for myelin pathology than conventional imaging methods. As a result, there is considerable interest in exploiting MT contrast to assay changes in myelination associated with a number of diseases [e.g., multiple sclerosis (Catalaa et al., 2000; Filippi and Rocca, 2004; Gass et al., 1994; Kalkers et al., 2001) and neuropsychiatric diseases (Bruno et al., 2004; Kabani et al., 2002a, 2002b)].

MT contrast can be generated by applying an off-resonance radiofrequency (RF) prepulse to selectively saturate the spectrally broad macromolecular proton pool (Wolff and Balaban, 1989). This saturation then transfers to the free water proton pool via MT, resulting in a decrease in the observed free water signal. The magnitude of this effect can be characterized by a semi-quantitative metric known as the magnetization transfer ratio (Dousset et al., 1992): $MTR = 1 - S_{sat}/S_0$, where S_{sat} and S_0 are the observed signal intensities with and without the application of an MT saturation prepulse, respectively. Although the MTR has been shown to correlate with myelin content (Odrobina et al., 2005; Schmierer et al., 2004), it is also sensitive to the choice of experimental parameters such as RF power (Berry et al., 1999) as well as non-MT-specific NMR parameters such as tissue relaxation times (Henkelman et al., 1993). As a result, quantitative MT (qMT) approaches have been developed. These qMT approaches quantify distinct tissue characteristics (e.g., the size of the macromolecular pool, rate of MT exchange) rather than the combined effect of multiple tissue and/or acquisition parameters. As such, qMT measures are thought to yield more specific information on tissue composition than the MTR .

Pulsed saturation qMT imaging (Graham and Henkelman, 1997; Pike, 1996; Sled and Pike, 2000, 2001) has received considerable attention for application in humans in vivo because it allows for the rapid collection of qMT data within the hardware constraints of most clinical systems. This approach involves a steady-state, spoiled gradient-echo acquisition interleaved with an MT-preparation pulse. By collecting images over a range of MT pulse offset frequencies and/or powers and fitting the resulting data to a two-pool model of the MT effect, one can extract parameters such as the macromolecular to free pool size ratio (PSR) and the rate of MT exchange. Previous work has shown that the PSR is correlated with myelin content (Odrobina et al., 2005; Ou et al., 2009; Schmierer et al., 2007; Underhill et al., 2011). The relationship between the rate of MT exchange and underlying tissue composition is less clear; however, previous work has suggested that the rate of MT exchange may reflect changes within the myelin lipid structure (Smith et al., 2009).

Unfortunately, qMT imaging has not found widespread application in practice. This can be attributed in part to the long scan times (≈ 20 – 30 min for whole-brain imaging) required to collect images at multiple offset frequencies and/or powers. The number of total images required can be reduced by designing optimal sampling strategies (Cercignani and Alexander, 2006; Levesque et al., 2011) or by fixing certain model parameters in the fitting procedure (Underhill et al., 2009, 2011). Potentially more efficient strategies based upon

steady-state free-precession (SSFP) sequences (Garcia et al., 2010; Gloor et al., 2008) may also be employed.

As an alternative, or perhaps in combination with these strategies, one could translate qMT imaging approaches to higher field strengths. The resulting increase in SNR could then be used to obtain more reliable estimates of MT parameters or traded to reduce scan times and/or increase resolution. To date, qMT studies in humans in vivo have been primarily limited to 1.5 and 3.0 T and we are aware of only one report (Mougin et al., 2010) of MT parameters in the human brain in vivo at 7.0 T. The translation of pulsed saturation approaches to 7.0 T faces two primary challenges: *i*) RF power limitations [e.g., specific absorption ratio (SAR) limitations] and *ii*) transmit RF (B_1^+) and static magnetic field (B_0) inhomogeneities. SSFP-based approaches may also be limited at high field by banding artifacts associated with B_0 inhomogeneities. In contrast, selective inversion recovery (SIR) qMT imaging (Edzes and Samulski, 1977; Gochberg et al., 1997), which is based upon measuring the biexponential recovery of the free water pool in the presence of MT after an on-resonance inversion pulse, has been suggested (Dortch et al., 2011) to be less sensitive to these issues. Note that this approach is similar to the stimulated echo approach proposed by Ropele et al. (2003); therefore, both approaches may be well suited for qMT imaging at 7.0 T.

In this study, we have investigated the feasibility of using the SIR approach for high field qMT imaging of the human brain. More specifically, we have translated our previously published 3.0-T SIR protocol (Dortch et al., 2011) to 7.0 T with two significant modifications. First, we incorporated a novel B_1^+ - and ΔB_0 -insensitive composite inversion pulse to ensure a more uniform inversion of the free water pool over the whole brain. Second, we transitioned from a turbo-spin echo readout (TSE) to a turbo field-echo readout (TFE)—similar to an MP-RAGE sequence (Mugler and Brookeman, 1990)—as the former is susceptible to B_1^+ -related artifacts (due to imperfect refocusing) and is SAR-limited at high field. The TFE readout has the added benefit of covering k -space more efficiently than the TSE readout, which, in combination with some additional protocol optimization, allowed us to transition from a single-slice approach at 3.0 T to a whole-brain approach at 7.0 T (≈ 40 s/slice at $2.0 \times 2.0 \times 3.0$ mm³ resolution). Using this protocol, in vivo qMT data were obtained in the brains of 13 healthy volunteers at 7.0 T. To assess the reproducibility of the technique, six of the healthy volunteers were scanned twice. Additional numerical simulations were performed to determine the effect of TFE readout on our qMT parameter maps.

Theory

Consider free water (f) and macromolecular (m) proton pools between which MT can occur. Define unique equilibrium magnetizations (M_{0f} and M_{0m}), spin-lattice relaxation rates (R_{1f} and R_{1m}), and spin-spin relaxation rates (R_{2f} and R_{2m}) for each pool as well as an MT rate from the macromolecular to the free pool (k_{mf})—the rate in the other direction can be determined from $k_{fm} = k_{mf} M_{0m} / M_{0f}$. Assume MT of transverse magnetization to be negligible because of the short T_2 of the macromolecular pool. In this case, the transverse components of the macromolecular pool can be ignored. The time evolution of the remaining x , y , and z components of the magnetization vector $\mathbf{M} = [M_{xf} M_{yf} M_{zf} M_{zm}]^T$ during a constant amplitude RF pulse can be expressed in matrix form as (Portnoy and Stanis, 2007)

$$\frac{d\mathbf{M}(t)}{dt} = \mathbf{A}\mathbf{M}(t) + \mathbf{B}, \quad (1)$$

where

$$\mathbf{A} = \begin{bmatrix} -R_{2f} & \Delta\omega & -\omega_1 \sin\phi & 0 \\ -\Delta\omega & -R_{2f} & \omega_1 \cos\phi & 0 \\ \omega_1 \sin\phi & -\omega_1 \cos\phi & -(R_{1f} + k_{fm}) & k_{mf} \\ 0 & 0 & k_{fm} & -(R_{1m} + R_{RF} + k_{mf}) \end{bmatrix}, \quad (2)$$

$$\mathbf{B} = \begin{bmatrix} 0 \\ 0 \\ R_{1f}M_{0f} \\ R_{1m}M_{0m} \end{bmatrix},$$

$\Delta\omega$ is the frequency offset from resonance for the RF pulse, ω_1 is the frequency of precession about the RF pulse, and ϕ is the phase of the RF pulse in the transverse plane. The standard Bloch equations implicitly assume a Lorentzian lineshape, which is invalid for the macromolecular proton pool. As a result, the Bloch equations for the macromolecular pool have been replaced in Eq. (2) by a single longitudinal component whose saturation is governed by the rate $R+RF=\pi\omega_1^2g_m(\Delta\omega)$, where g_m is the lineshape function of the macromolecular pool. When applying off-resonance irradiation, a super-Lorentzian lineshape is typically used to model biological macromolecular protons (Morrison et al., 1995). Because the super-Lorentzian exhibits an on-resonance singularity, Gaussian (Gochberg and Gore, 2007) or super-Lorentzian functions extrapolated from a 1 kHz offset (Gloor et al., 2008) are typically used to model the macromolecular pool lineshape pool during on-resonance irradiation.

The general solution to this system of equations can be expressed as

$$\mathbf{M}(t) = \exp(\mathbf{A}t) \mathbf{M}(0) + [\exp(\mathbf{A}t) - \mathbf{I}] \mathbf{A}^{-1} \mathbf{B}, \quad (3)$$

where $\mathbf{M}(0)$ is the initial condition of the system and \mathbf{I} is an identity matrix. The same expression can be used to describe the system during free precession (i.e., when $\omega_1=0$). In this case, the solution can be further simplified by noting that the z -component is decoupled from the x - and y -components, resulting in the following expression for the longitudinal magnetization vector $\mathbf{M}_z = [M_{zf} M_{zm}]^T$

$$\mathbf{M}_z(t) = \exp(\mathbf{A}_z t) \mathbf{M}(0) + [\mathbf{I} - \exp(\mathbf{A}_z t)] \mathbf{M}_0, \quad (4)$$

where $\mathbf{M}_0 = [M_{0f} M_{0m}]^T$ and \mathbf{A}_z is the lower-right quadrant of \mathbf{A} with $R_{RF}=0$. Expanding the matrix exponentials in this expression yields

$$\mathbf{M}_z(t) = \mathbf{U} \begin{bmatrix} e^{-\lambda^+ t} & 0 \\ 0 & e^{-\lambda^- t} \end{bmatrix} \mathbf{U}^{-1} \mathbf{M}(0) + \left(\mathbf{I} - \mathbf{U} \begin{bmatrix} e^{-\lambda^+ t} & 0 \\ 0 & e^{-\lambda^- t} \end{bmatrix} \mathbf{U}^{-1} \right) \mathbf{M}_0, \quad (5)$$

where $\lambda^{+/-}$ are the negative eigenvalues of \mathbf{A}_z and \mathbf{U} is a matrix whose columns are the corresponding eigenvectors. From Eq. (5), it can be seen that M_{zf} recovers as a biexponential function governed by the fast and slow rate constants λ^+ and λ^- , respectively, during free precession. As described below, one can obtain estimates of qMT parameters (e.g., PSR and k_{mf}) by measuring this biexponential recovery.

Methods

Pulse sequence

The SIR qMT sequence (Fig. 1) used herein is similar to the inversion recovery sequence used to measure T_1 with two modifications. First, short inversion times (≈ 10 ms or less) are sampled in order to capture the fast-recovering λ^+ component of the biexponential recovery. Second, a T_2 -selective inversion pulse is applied. This is achieved via a low power inversion pulse whose duration is much longer than the T_2 of the macromolecular pool ($T_{2m} \approx 10 \mu\text{s}$) and much shorter than the T_2 of the free water pool ($T_{2f} \approx 10\text{--}100$ ms). Ideally, this pulse inverts M_{zf} with minimal saturation of M_{zm} . In other words, this pulse maximizes the difference between the pools and, in turn, the sensitivity of the signal to MT. This is followed by a variable duration inversion recovery period to sample the transient biexponential recovery of M_{zf} and a center-out TFE readout (SIR-TFE) to efficiently sample k -space. For inversion recovery acquisitions, a predelay time $t_d \approx 5/\lambda^-$ is commonly employed to ensure full recovery of M_{zf} . However, if one can assume that the longitudinal magnetization of both pools is approximately zero at the end of the readout, the effect of a shorter predelay period can be accounted for in the signal model, allowing one to reduce t_d (and scan times) without biasing the estimated parameters. This assumption has been previously shown to hold true for a TSE readout (Gochberg and Gore, 2007); however, this cannot be assumed for the TFE readout employed herein. As a result, we empirically designed a train of RF pulses [number of pulses=32, $\alpha=135^\circ$, pulse spacing=20 ms, pulse train duration (t_{sat})=620 ms] to saturate both pools following the TFE readout. To assess the effect of this pulse train on the longitudinal magnetization of both pools, numerical simulations were performed via Eq. (3) and the following parameters: $R_{1m}=R_{1f}=0.8 \text{ s}^{-1}$, $T_{2m}=10 \mu\text{s}$ (Gaussian lineshape), $T_{2f}=60$ ms, $k_{mf}=15 \text{ s}^{-1}$, and $PSR=15\%$. The results from these simulations indicate that this pulse train saturates both pools [$M_{zf}(t_{sat})/M_{0f}$ 0.01 and $M_{zm}(t_{sat})/M_{0m}$ 0.06] over the range of expected B_1^+ values ($B_{1,actual}^+/B_{1,nominal}^+=0.3\text{--}1.0$) in the human brain at 7.0 T [n.b., the manufacturer-provided power optimization tended to yield a mean $B_{1,actual}^+/B_{1,nominal}^+ < 1.0$ (Moore et al., 2010)].

Plugging the initial condition of $\mathbf{M}_z(t_f=0)=\mathbf{0}$ into Eq. (4), signal equations can be generated for the predelay period of the SIR-TFE sequence. The ending values for this period can then be used as the initial condition for the inversion recovery period, taking account for the effect of the inversion pulse

$$\mathbf{M}_z(t^+) = \mathbf{S} \mathbf{M}_z(t^-), \quad (6)$$

where \mathbf{S} is a diagonal matrix with elements that account for the inversion of the free pool ($S_f=-1$ denotes complete inversion) and the saturation of the macromolecular pool ($S_m=1$ denotes no saturation) and t^{\pm} is the time immediately before/after the pulse. This yields the final expression for the evolution of \mathbf{M}_z during the SIR period of the sequence

$$\mathbf{M}_z(t_i, t_d) = (\exp(\mathbf{A}_z t_i) \mathbf{S} [\mathbf{I} - \exp(\mathbf{A}_z t_d)] + [\mathbf{I} - \exp(\mathbf{A}_z t_i)]) \mathbf{M}_0. \quad (7)$$

In addition to these pulse sequence modifications, a novel 64-element composite inversion pulse was designed and employed herein to ensure a uniform inversion of M_{zf} over the range of B_1^+ and ΔB_0 values previously measured in the human brain at 7.0 T (Moore et al., 2010). The optimization procedure (Moore et al., 2010) tended to produce high power pulses with suboptimal T_2 -selectivity. As a result, we included an additional RF power constraint into the procedure, which was weighted against the uniform inversion constraint. The resulting amplitudes and phases of the subpulses are shown in Fig. 2. To evaluate the pulse's performance, S_f and S_m were estimated from Eq. (6) by propagating Eq. (3) through each of

the 64 subpulses [neglecting T_1 relaxation and MT during the pulse and assuming a Gaussian macromolecular pool lineshape with $T_{2m}=10\ \mu\text{s}$ (Gochberg and Gore, 2007)]. From this procedure, the pulse is predicted to yield a uniform inversion of M_{zf} over a wide range of B_1^+ and ΔB_0 values without complete saturation of M_{zm} .

Numerical simulations

The TFE readout employed herein effectively blurs the image along the phase-encoding direction according to its readout point-spread function (PSF), which is a complex function of the sequence timings and the NMR parameters of the tissue (Constable and Gore, 1992). If the readout PSF is constant as a function of t_i , then its effect will be to simply blur the final MT parameter maps. If, however, the readout PSF changes as a function of t_i , each image will be blurred to a different degree, potentially biasing the final parameter maps.

To evaluate this effect, the SIR-TFE signal arising from a one-dimensional (1D) test object was numerically simulated. As shown in Fig. 3, MT parameters were defined for test object regions representing white matter (WM), gray matter (GM), and cerebrospinal fluid (CSF). For each region and t_i , the signal evolution during each RF pulse and precession period of the TFE readout was simulated from Eq. (3) with the imaging parameters in the Data acquisition section—using $\mathbf{M}_z(t_i)$ from Eq. (7) as the initial condition and replacing each time-varying excitation pulse with a constant amplitude pulse of equivalent flip angle or root-mean-squared power (Ramani et al., 2002) for the free water or macromolecular pool, respectively. Complete spoiling of transverse magnetization was assumed prior to each RF pulse. The resulting M_{zf} immediately after each RF pulse was taken to represent the signal as a function of echo number. The signal was then re-ordered to account for the k -space trajectory and SENSE acceleration used, and the resulting re-ordered signal was taken to represent a k -space filter. To apply the k -space filters to the 1D test object, each uniform object region was Fourier transformed into k -space, multiplied by its corresponding k -space filter, and inverse Fourier transformed back into image space. The resulting object regions were then summed to generate the final blurred 1D object at each t_i . Finally, to assess the effect of the TFE readout on qMT parameter maps, the magnitude of the blurred test object signal at each voxel was fit to the M_{zf} component of Eq. (7) as described in the Data analysis section.

Subjects

MRI was performed on thirteen healthy volunteers (22–37 years old, 10 male, 3 female). To test reproducibility, six of the healthy volunteers were asked to undergo a second MRI scan at least two weeks after the first session. The study was approved by our local institutional review board, and signed consent was obtained prior to all examinations.

Data acquisition

Imaging was performed using a 7.0-T, Philips Achieva MR scanner (Philips Healthcare, Best, The Netherlands). A quadrature volume coil was used for excitation and a 32-channel head coil (Nova Medical, Wilmington, MA, USA) was used for signal reception. For qMT imaging, SIR-TFE data were collected in each subject using the general pulse sequence shown in Fig. 1.

An initial experiment was performed in one healthy volunteer to determine the effect of the post-TFE saturation train and predelay time t_d on the qMT parameter maps. For this initial experiment, SIR-TFE data were acquired in a single 5-mm axial slice with and without the post-TFE saturation train (see Fig. 1, shaded area labeled SAT) over a range of t_d values (0.125–10 s). Additional imaging parameters included: t_i logarithmically spaced between 6 ms and 2 s (15 values) and $t_f=10$ s, TFE echoes per shot=53, TFE pulse-to-pulse interval (τ)/

TE/ α =2.8 ms/1.4 ms/15°, SENSE factor=2, field-of-view=212×212 mm², resolution=2.0×2.0 mm², and number of signal acquisitions averaged (NSA)=2.

Based upon the results of this experiment along with previous numerical simulations (Gochberg and Gore, 2007), a t_d of 2.5 s was chosen to balance the scan time and SNR constraints for whole-brain SIR-TFE imaging. Whole-brain qMT data were acquired in 12 volunteers (six scanned twice) via a three-dimensional (3D) SIR-TFE sequence using the previously listed parameters except: t_i logarithmically spaced between 6 ms and 2 s (13 values) and t_f =8 s, SENSE factor=4 (2 anterior–posterior, 2 superior–inferior), field-of-view=212×212×90 mm³, resolution=2.0×2.0×3.0 mm³, and NSA=1. This resulted in an acquisition time≈19 min for 30 slices.

Recall that the signal model [Eq. (7)] has terms (S_f and S_m) that account for the effect of the inversion pulse on the free and macromolecular pool magnetizations. S_f was included as a free parameter in the fit as described in the Data analysis section, while S_m was numerically estimated as described in the Pulse sequence section. Because S_m is sensitive to B_1^+ (see Fig. 2d), this numerical estimation required an independent measurement of B_1^+ . As a result, B_1^+ was estimated in same volume as the SIR-TFE data using the actual flip angle imaging (AFI) method (Yarnykh, 2007) with TR₁/TR₂=125/25 ms and a 60° slab-selective excitation pulse (asymmetric sinc pulse with Gaussian apodization).

Data analysis

All data analyses were performed in MATLAB (Mathworks, Natick, MA). Prior to data fitting, each SIR-TFE and AFI volume was co-registered to the SIR-TFE volume acquired at t_f =110 ms (middle value) using a 3D rigid body registration based upon normalized mutual information (Viola and Wells, 1997). Following co-registration, automatic brain extraction was performed (Smith, 2002) and qMT parameter maps were calculated in each volunteer. The SIR-TFE signal model described in Eq. (7) has seven independent parameters: R_{1m} , R_{1f} , S_m , S_f , M_{0f} , $PSR=M_{0m}/M_{0f}$ and k_{mf} ($k_{fm}=k_{mf}PSR$). As is the case with pulsed saturation methods, the signal dependence on R_{1m} for SIR data is weak (Li et al., 2010). Therefore, R_{1m} was set equal to R_{1f} for fitting purposes. The parameter S_m was numerically estimated for each voxel. This required an independent estimate of the actual flip angle in each voxel (α_{actual}), which was calculated from the AFI data using the following relationship (Yarnykh, 2007):

$$\alpha_{actual} = \cos^{-1} \left(\frac{m - 1}{n - r} \right), \quad (8)$$

where $n=TR_2/TR_1$, $r=S(TR_2)/S(TR_1)$, and S is the signal intensity. The resulting α_{actual} map was smoothed with a 10×10×9 mm³ moving-average filter to minimize the impact of imaging artifacts. Following this operation, the flip angle values were converted to $B_{1,actual}^+$ values for the composite inversion pulse (see Fig. 2a) and S_m was estimated using the procedure described in the Pulse sequence section (see Fig. 2d). The remaining five parameters (R_{1f} , S_f , M_{0f} , k_{mf} and PSR) were estimated for each voxel by fitting SIR-TFE data (14 t_i values) to the M_{zf} component of Eq. (7) in a least-squares sense using the procedure described in Dortch et al. (2011).

SIR-TFE data had a mean SNR per voxel of 180±50 (range=60–320) within the defined ROIs, where SNR is defined as M_{0f} divided by the standard deviation (SD) of the residuals of the fit. Monte Carlo simulations, similar to those described by Li et al. (2010), were performed to predict the uncertainty of the fit parameters at these SNR levels. The t_i and t_d values listed above were used for these simulations. Additional simulation parameters included: $R_{1m}=R_{1f}=0.8 \text{ s}^{-1}$, $k_{mf}=15 \text{ s}^{-1}$, $PSR=15\%$, $S_m=0.7$, and $S_f=-0.95$. Over an SNR

range of 60–320, the SDs of the fit PSR , R_{1f} and k_{mf} values were 0.4–2.2%, 0.01–0.03 s⁻¹, and 0.9–5.5 s⁻¹, respectively. This suggests that PSR and R_{1f} can be robustly determined from the in vivo brain data collected herein. Consistent with previous studies (Li et al., 2010), the uncertainty in k_{mf} is expected to be much larger, especially in lower SNR regions.

Following this fitting procedure, qMT parameter maps were smoothed with a locally-adaptive Gaussian filter (kernel size=10×10×9 mm³, full width at half maximum=1/2 kernel size) to remove outliers that tended to occur at tissue boundaries. To perform this operation, each filtered map was subtracted from the raw parameter map, and outliers were defined as voxels whose value was three standard deviations above the mean difference across all voxels. For these outliers, the value in the raw parameter map was replaced with the value in the filtered map. This process was iterated until the number of outliers was less than the expected value (0.3% of the total number of voxels).

Statistics

Mean qMT parameters (PSR , R_{1f} and k_{mf}) were calculated within the following regions-of-interest (ROI): head of the caudate, putamen, thalamus, genu and splenium of the corpus callosum, internal capsule, corona radiata, occipital WM, and frontal WM. Statistical comparisons were performed on the mean ROI values to evaluate each parameter's *i*) variation across ROIs (i.e., regional differences), *ii*) variation and reproducibility across time, and *iii*) variation across volunteers. To compare parameters across WM regions, a non-parametric Wilcoxon rank-sum test was performed, with a $p < 0.05$ deeming a significant difference between ROI values. To evaluate the test–retest reproducibility of each parameter, a Bland–Altman (BA) analysis was performed. For the BA analysis, the mean difference and the limits of agreement (LOA=mean difference±1.96*SD) were tabulated across scans for all ROIs. Additionally, a Wilcoxon signed-rank test was performed between the test and retest parameter values for each ROI, with a $p > 0.05$ indicating a non-significant difference between scans at each time point. To assess the test–retest variability of each parameter within each ROI, the coefficient of variation was calculated from:

$CV_{\text{retest}} = S / (M \sqrt{2}) * 100$, where S is the SD of the test–retest difference across subjects, M is the mean value across all test–retest scans and subjects, and the $\sqrt{2}$ term accounts for the propagation of uncertainty from the difference operation. The across-cohort variability of each parameter within each ROI was also assessed via: $CV_{\text{cohort}} = S/M * 100$, where S is the SD across the cohort and M is mean value across the cohort. All values are reported as the mean±SD unless otherwise stated.

Results

The results of the numerical simulations designed to assess the effect of TFE readout on qMT parameter maps are shown in Fig. 3. In Fig. 3a, the evolution of M_{zf} during the TFE readout is shown for WM as a function of t_f . Note that this evolution is related to the k -space filter of the readout. It can be seen that the shape (width and rate of decay) of the k -space filter changes as a function of t_f , which manifests as a change in object blurring as a function of t_f . The effect of this on the qMT parameter maps is shown in Figs. 3b–d. It can be seen that the resulting qMT parameter maps are smoothed in the phase-encoding direction with little bias in the fit parameters. It should be noted, however, that PSR values were slightly underestimated in the WM region of the 1D test object. Additional simulations indicated that this bias increased as the size of the WM region decreased.

Fig. 4 displays PSR maps acquired with and without application of the post-TFE saturation train (see the SAT region in Fig. 1) as a function of t_d . For scans with the saturation train, the fit PSR values at shorter t_d values were nearly identical to those at full recovery ($t_d=10$

s). Without this train, small deviations in PSR were observed at $t_d=2.5$ s; and these were more pronounced at $t_d=1.25$ s. Thus, the post-TFE saturation train allows for reduction of t_d (and scan times) with minimal parameter bias.

Representative 3D SIR-TFE data are shown in Fig. 5. Fig. 5a shows a single slice at the level of the lateral ventricles acquired at six of 14 t_j values. Note the characteristic center brightening due to B_1^+ inhomogeneities. Fig. 5b shows data from a single voxel in the genu of the corpus callosum and the corresponding model fit. Note the agreement between the SIR-TFE data and the biexponential model described by Eq. (7). Additionally, note the deviation from monoexponential recovery, which is especially evident at the shortest inversion times.

Based upon these fits, maps of qMT parameters were generated. Recall that these maps were filtered to reduce the impact of outliers. Fig. 6 displays representative qMT parameter maps without filtering, with the previously described locally-adaptive Gaussian filter, and with a global Gaussian filter. The locally-adaptive and global filters both removed outliers in the parameter maps (see arrow in the top row and the masks in the bottom row); however, the locally filtered maps were blurred to a much smaller degree. As a result, we employed the locally-adaptive approach herein. For all parameter maps, 14% of all voxels in the post-brain-extraction volume were smoothed using this approach. However, as seen in the bottom row of Fig. 6, a majority of these voxels were located along the brain surface or within the CSF.

Fig. 7 displays results from four representative slices in one healthy subject. The qMT parameters were uniform over most of the volume despite the presence of large ΔB_0 and/or B_1^+ field inhomogeneities (as indicated by the heterogeneity in the S_m maps). There does, however, appear to be some bias in the qMT parameter values in midbrain slices (black arrow), which typically (Moore et al., 2010) exhibit the largest field inhomogeneities and the lowest SNR. Nevertheless, these data suggest that robust qMT parameter mapping can be achieved throughout most of the brain using the 3D SIR-TFE protocol described herein.

ROIs were defined in a number of WM and GM regions as shown in Fig. 8. The boxplots in the top row of Fig. 9 display the mean ROI qMT parameters over the 12 healthy volunteers. For PSR , the mean value across all WM ROIs ($17.6 \pm 1.3\%$) was higher than the values across all GM ROIs ($10.3 \pm 1.6\%$). Additionally, heterogeneity within WM PSR values was observed, but should be interpreted with caution due to the effect of multiple comparisons. Nevertheless, differences between the following regions were detected: *i*) the genu of the corpus callosum and occipital WM ($p=0.026$), *ii*) the genu of the corpus callosum and the corona radiata ($p=0.026$), *iii*) frontal and occipital WM ($p=0.041$), and *iv*) frontal WM and the corona radiata ($p=0.041$). Fit k_{mf} values were higher in GM ($24.4 \pm 4.4 \text{ s}^{-1}$) than in WM ($14.5 \pm 1.5 \text{ s}^{-1}$). Additionally, note the large, biased k_{mf} values in and around areas containing CSF, which is likely a consequence of the weak dependence of the signal on k_{mf} when $PSR \approx 0$ (see the simulated data in Fig. 3c). For $R_{1\rho}$, differences between WM ($0.73 \pm 0.03 \text{ s}^{-1}$) and GM ($0.58 \pm 0.05 \text{ s}^{-1}$) values were also observed. The boxplots in Fig. 9 give an indication of the variability of each parameter across the healthy cohort. To quantify this, the coefficient of variation was tabulated for each ROI, and the mean value across all ROI is given in Table 1. From this, it can be seen that the mean CV_{cohort} was $<10\%$ for all of the qMT parameters, which is not surprising given the small age range of the healthy cohort scanned herein.

BA plots of the observed difference in mean ROI qMT parameters between scans are shown in the bottom row of Fig. 9; and the results from this analysis are given numerically in Table 1. The mean difference for all ROIs across scans was close to zero for PSR (0.0%), k_{mf} (1.2

s^{-1}), and $R_{1f}(0.01 s^{-1})$, indicating a lack of bias and reasonable reproducibility. To further test this, a Wilcoxon signed-rank test was performed on the test–retest parameter values in each ROI. At the $p=0.05$ level, no significant difference was observed between test and retest qMT parameters in any of the ROIs except for k_{mf} in the genu of the corpus callosum ($p=0.031$). The test–retest coefficient of variation (CV_{retest}) was also tabulated for each metric to further assess each parameter’s variability across time. As shown in Table 1, the relative CV_{retest} values were consistent with the corresponding CV_{cohort} values, with k_{mf} exhibiting the highest variability. In terms of absolute CV values, the test–retest variability was approximately 20% lower than the across cohort variability.

Discussion

This study demonstrates the feasibility of performing whole-brain qMT measurements in the human brain in vivo at high field. Pulsed saturation and SSFP-based approaches are difficult to implement at high field due to RF power limitations and/or magnetic field (B_1^+ and ΔB_0) inhomogeneities. In this study, we employed the SIR qMT approach, which has been suggested to be less sensitive to these issues. The biggest obstacles to overcome were *i*) the effect of B_1^+ and ΔB_0 inhomogeneities on the inversion pulse and the readout and *ii*) the long scan times associated with SIR imaging. The former of these was mitigated by developing a novel B_1^+ and ΔB_0 insensitive inversion composite pulse (Fig. 2) and employing a low-flip angle TFE readout; the latter was mitigated by the efficiency of the TFE readout along with additional protocol optimization (e.g., reducing the number of t_I values to 14, applying SENSE acceleration in two directions). Together this resulted in a robust (Fig. 9), whole-brain qMT imaging protocol with a scan time of less than 20 min.

Previous qMT imaging studies at lower field strengths (Dortch et al., 2011; Garcia et al., 2010; Gloor et al., 2008; Ropele et al., 2003; Sled and Pike, 2001; Sled et al., 2004; Yarnykh and Yuan, 2004) have reported PSR values in the range of 11–16% and 5–9% for WM and GM structures, respectively [$PSR=F$ using the notation of Sled and Pike (2000, 2001) and M_{0b} using the notation of Henkelman et al. (1993)]. The PSR values presented herein (WM: 15–20%, GM: 9–13%) were approximately 25% higher. PSR should be independent of field strength, so these differences may be related to the SIR-TFE sequence. As previously discussed, we modified the inversion pulse and readout of our 3.0-T SIR-FSE sequence to perform qMT imaging at 7.0 T. The effect of the TFE readout on the fit qMT parameters was assessed via numerical simulations and was found to result in little bias in PSR (Fig. 3). However, it should be noted that our previous report at 3.0 T employed a much longer TE (74 ms) than was employed herein (1.4 ms). Previous work (Bjarnason et al., 2005; Stanisz et al., 1999) has demonstrated that MT contrast is TE-dependent in WM due to the microanatomical compartmentation of water into myelin and nonmyelin water spaces. As a result, it is reasonable to assume that PSR may also exhibit a TE-dependence. In terms of the inversion pulse, we recognize that PSR is sensitive to the macromolecular pool lineshape and T_{2m} assumptions used in the numerical estimation of S_m . Similar to our previous studies (Dortch et al., 2011; Gochberg and Gore, 2007), we modeled the macromolecular pool using a Gaussian lineshape ($T_{2m}=10 \mu s$) because the Super-Lorentzian exhibits an on-resonance singularity. Previous work using a 1-ms block inversion pulse at 3.0 T (Dortch et al., 2011) found that this was a reasonable approximation; however, this may not be true for the longer (5.5 ms), higher power composite inversion pulse employed herein. Additional work is needed to explore the field- and TE-dependence of PSR values obtained via the SIR technique. Nevertheless, the reported regional variation in PSR values was consistent with previous qMT imaging studies (Dortch et al., 2011; Garcia et al., 2010; Sled et al., 2004; Underhill et al., 2009); and additional SIR-TFE studies in bovine serum albumin phantoms at 7.0 T (data not shown) found a linear relationship between macromolecular content and PSR . Thus, we postulate that the regional differences in PSR values reported herein are

driven primarily by regional differences in myelin content, although the absolute values may be systematically larger than reported by other techniques.

Previous pulsed saturation and SSFP-based studies (Garcia et al., 2010; Gloor et al., 2008; Ropele et al., 2003; Sled and Pike, 2001; Sled et al., 2004; Yarnykh and Yuan, 2004) report k_{mf} values [$k_{mf}=k_f F$ using the notation of Sled and Pike (2000, 2001); $k_{mf}=R$ when $M_0=1$ using the notation of Henkelman et al. (1993)] in the range of 20–40 s^{-1} across the brain. A previous SIR study (Dortch et al., 2011) at 3.0 T reports k_{mf} values that are approximately 2-fold slower (10–15 s^{-1}) with values that are slower in WM than GM, which is consistent with the results presented herein. The discrepancies between techniques are not surprising given the reported difficulty of using pulsed saturation to determine k_{mf} (Portnoy and Stanisiz, 2007). In terms of the current study, it should be noted that k_{mf} showed the largest variability of the qMT parameters, which is consistent with the results from the Monte Carlo simulations. We do not expect this to be a significant drawback as k_{mf} has been shown to be insensitive to the pathological changes in spinal cord WM (Smith et al., 2009).

While there have been no previous reports of R_{1f} in human brain at 7.0 T, it can be shown that the observed T_1 typically reported is $\approx 1/R_{1f}$. Using this relationship, the mean WM and GM observed T_1 values were 1372 and 1724 ms, respectively, which are within the range of previously reported values in human brain at 7.0 T (Wright et al., 2008). As expected, we noted a significant correlation between R_{1f} and PSR in the healthy human brain (data not shown); however, T_1 is sensitive to overall tissue composition [e.g., water content (Kiricuta and Simplaceanu, 1975)] and is believed to be a less specific marker for myelin in WM.

The increased SNR available at 7.0 T was used here to decrease scan time (≈ 40 s/slice) and increase resolution ($2 \times 2 \times 3$ mm³) relative to our 3.0-T protocol. Moving forward, it may be advantageous to look at higher resolution protocols. If we assume that all imaging parameters are the same, increasing the resolution to $1 \times 1 \times 3$ mm³ would result in an approximately two-fold decrease in SNR (≈ 70 at thermal equilibrium, assuming we increase the number of acquired points to hold the field-of-view constant). Based upon previous simulation work (Li et al., 2010) as well as the simulation work presented herein, this would be sufficient to robustly fit qMT parameters over most of the brain. Thus, it appears that high-resolution qMT imaging may be feasible in the human brain in vivo at 7.0 T using a protocol similar to that described herein.

Conclusions

The results of this study demonstrate the feasibility of performing qMT imaging in human brain in vivo at high field. The developed SIR-TFE protocol allowed for whole-brain qMT imaging in less than 20 min. In healthy subjects, intra-subject reliability (i.e., test–retest) was demonstrated despite large ΔB_0 and B_1^+ variations. Additionally, a high level of inter-subject reproducibility was demonstrated for the qMT parameters. Future work includes investigating high-resolution protocols to look at cortical features of qMT parameters and application of the approach in a cohort of multiple sclerosis patients.

Acknowledgments

This work was supported by NIH/NBIB K01 EB009120 (SAS), NIH T32 EB001628 (JCG), NIH EB00461 (JCG), and Vanderbilt Bridge Funding (DFG).

References

- Berry I, Barker G, Barkhof F, Campi A, Dousset V, Franconi J, Gass A, Schreiber W, Miller D, Tofts P. A multicenter measurement of magnetization transfer ratio in normal white matter. *J. Magn. Reson. Imaging*. 1999; 9:441–446. [PubMed: 10194715]
- Bjarnason T, Vavasour I, Chia C, Mackay A. Characterization of the NMR behavior of white matter in bovine brain. *Magn. Reson. Med*. 2005; 54:1072–1081. [PubMed: 16200557]
- Bruno SD, Barker GJ, Cercignani M, Symms M, Ron MA. A study of bipolar disorder using magnetization transfer imaging and voxel-based morphometry. *Brain*. 2004; 127:2433–2440. [PubMed: 15469950]
- Catalaa I, Grossman RI, Kolson DL, Udupa JK, Nyul LG, Wei L, Zhang X, Polansky M, Mannon LJ, McGowan JC. Multiple sclerosis: magnetization transfer histogram analysis of segmented normal-appearing white matter. *Radiology*. 2000; 216:351–355. [PubMed: 10924552]
- Cercignani M, Alexander D. Optimal acquisition schemes for in vivo quantitative magnetization transfer MRI. *Magn. Reson. Med*. 2006; 56:803–810. [PubMed: 16902982]
- Constable RT, Gore JC. The loss of small objects in variable TE imaging: implications for FSE, RARE, and EPI. *Magn. Reson. Med*. 1992; 28:9–24. [PubMed: 1435225]
- Dortch RD, Li K, Gochberg DF, Welch EB, Dula AN, Tamhane AA, Gore JC, Smith SA. Quantitative magnetization transfer imaging in human brain at 3 T via selective inversion recovery. *Magn. Reson. Med*. 2011; 66:1346–1352. [PubMed: 21608030]
- Dousset V, Grossman RI, Ramer KN, Schnell MD, Young LH, Gonzalez-Scarano F, Lavi E, Cohen JA. Experimental allergic encephalomyelitis and multiple sclerosis: lesion characterization with magnetization transfer imaging. *Radiology*. 1992; 182:483–491. [PubMed: 1732968]
- Edzes HT, Samulski ET. Cross relaxation and spin diffusion in the proton NMR of hydrated collagen. *Nature*. 1977; 265:521–523. [PubMed: 834303]
- Filippi M, Rocca MA. Magnetization transfer magnetic resonance imaging in the assessment of neurological diseases. *J. Neuroimaging*. 2004; 14:303–313. [PubMed: 15358949]
- Garcia M, Gloor M, Wetzel SG, Radue E-W, Scheffler K, Bieri O. Characterization of normal appearing brain structures using high-resolution quantitative magnetization transfer steady-state free precession imaging. *NeuroImage*. 2010; 52:532–537. [PubMed: 20430101]
- Gass A, Barker GJ, Kidd D, Thorpe JW, MacManus D, Brennan A, Tofts PS, Thompson AJ, McDonald WI, Miller DH. Correlation of magnetization transfer ratio with clinical disability in multiple sclerosis. *Ann. Neurol*. 1994; 36:62–67. [PubMed: 8024264]
- Gloor M, Scheffler K, Bieri O. Quantitative magnetization transfer imaging using balanced SSFP. *Magn. Reson. Med*. 2008; 60:691–700. [PubMed: 18727085]
- Gochberg D, Gore J. Quantitative magnetization transfer imaging via selective inversion recovery with short repetition times. *Magn. Reson. Med*. 2007; 57:437–441. [PubMed: 17260381]
- Gochberg D, Kennan R, Gore J. Quantitative studies of magnetization transfer by selective excitation and T_1 recovery. *Magn. Reson. Med*. 1997; 38:224–231. [PubMed: 9256101]
- Graham SJ, Henkelman RM. Understanding pulsed magnetization transfer. *J. Magn. Reson. Imaging*. 1997; 7:903–912. [PubMed: 9307918]
- Henkelman R, Huang X, Xiang Q, Stanisz G, Swanson S, Bronskill M. Quantitative interpretation of magnetization transfer. *Magn. Reson. Med*. 1993; 29:759–766. [PubMed: 8350718]
- Kabani NJ, Sled JG, Chertkow H. Magnetization transfer ratio in mild cognitive impairment and dementia of Alzheimer's type. *NeuroImage*. 2002a; 15:604–610. [PubMed: 11848703]
- Kabani NJ, Sled JG, Shuper A, Chertkow H. Regional magnetization transfer ratio changes in mild cognitive impairment. *Magn. Reson. Med*. 2002b; 47:143–148. [PubMed: 11754453]
- Kalkers NF, Hintzen RQ, van Waesberghe JH, Lazeron RH, van Schijndel RA, Ader HJ, Polman CH, Barkhof F. Magnetization transfer histogram parameters reflect all dimensions of MS pathology, including atrophy. *J. Neurol. Sci*. 2001; 184:155–162. [PubMed: 11239950]
- Kiricuta IC Jr, Simplaceanu V. Tissue water content and nuclear magnetic resonance in normal and tumor tissues. *Cancer Res*. 1975; 35:1164–1167. [PubMed: 1120306]
- Koenig SH. Cholesterol of myelin is the determinant of gray–white contrast in MRI of brain. *Magn. Reson. Med*. 1991; 20:285–291. [PubMed: 1775053]

- Kucharczyk W, Macdonal P, Stanisz G, Henkelman R. Relaxivity and magnetization transfer of white matter lipids at MR imaging: importance of cerebroside and pH. *Radiology*. 1994; 192:521–529. [PubMed: 8029426]
- Levesque IR, Sled JG, Pike GB. Iterative optimization method for design of quantitative magnetization transfer imaging experiments. *Magn. Reson. Med*. 2011; 66:635–643. [PubMed: 21748796]
- Li K, Zu Z, Xu J, Janve VA, Gore JC, Does MD, Gochberg DF. Optimized inversion recovery sequences for quantitative T_1 and magnetization transfer imaging. *Magn. Reson. Med*. 2010; 64:491–500. [PubMed: 20665793]
- Moore J, Jankiewicz M, Zeng H, Anderson AW, Gore JC. Composite RF pulses for B_1^+ -insensitive volume excitation at 7 Tesla. *J. Magn. Reson*. 2010; 205:50–62. [PubMed: 20451430]
- Morrison C, Stanisz G, Henkelman RM. Modeling magnetization transfer for biological-like systems using a semi-solid pool with a super-Lorentzian lineshape and dipolar reservoir. *J. Magn. Reson. B*. 1995; 108:103–113. [PubMed: 7648009]
- Mougin OE, Coxon RC, Pitiot A, Gowland PA. Magnetization transfer phenomenon in the human brain at 7 T. *NeuroImage*. 2010; 49:272–281. [PubMed: 19683581]
- Mugler JP III, Brookeman JR. Three-dimensional magnetization-prepared rapid gradient-echo imaging (3D MP RAGE). *Magn. Reson. Med*. 1990; 15:152–157. [PubMed: 2374495]
- Odrobina E, Lam T, Pun T, Midha R, Stanisz G. MR properties of excised neural tissue following experimentally induced demyelination. *NMR Biomed*. 2005; 18:277–284. [PubMed: 15948233]
- Ou X, Sun SW, Liang HF, Song SK, Gochberg DF. The MT pool size ratio and the DTI radial diffusivity may reflect the myelination in shiverer and control mice. *NMR Biomed*. 2009; 22:480–487. [PubMed: 19123230]
- Pike GB. Pulsed magnetization transfer contrast in gradient echo imaging: a two-pool analytic description of signal response. *Magn. Reson. Med*. 1996; 36:95–103. [PubMed: 8795027]
- Portnoy S, Stanisz GJ. Modeling pulsed magnetization transfer. *Magn. Reson. Med*. 2007; 58:144–155. [PubMed: 17659607]
- Ramani A, Dalton C, Miller DH, Tofts PS, Barker GJ. Precise estimate of fundamental in-vivo MT parameters in human brain in clinically feasible times. *Magn. Reson. Imaging*. 2002; 20:721–731. [PubMed: 12591568]
- Ropele S, Seifert T, Enzinger C, Fazekas F. Method for quantitative imaging of the macromolecular ^1H fraction in tissues. *Magn. Reson. Med*. 2003; 49:864–871. [PubMed: 12704769]
- Schmierer K, Scaravilli F, Altmann D, Barker G, Miller D. Magnetization transfer ratio and myelin in postmortem multiple sclerosis brain. *Ann. Neurol*. 2004; 56:407–415. [PubMed: 15349868]
- Schmierer K, Tozer DJ, Scaravilli F, Altmann DR, Barker GJ, Tofts PS, Miller DH. Quantitative magnetization transfer imaging in postmortem multiple sclerosis brain. *J. Magn. Reson. Imaging*. 2007; 26:41–51. [PubMed: 17659567]
- Sled JG, Pike GB. Quantitative interpretation of magnetization transfer in spoiled gradient echo MRI sequences. *J. Magn. Reson*. 2000; 145:24–36. [PubMed: 10873494]
- Sled JG, Pike GB. Quantitative imaging of magnetization transfer exchange and relaxation properties in vivo using MRI. *Magn. Reson. Med*. 2001; 46:923–931. [PubMed: 11675644]
- Sled JG, Levesque I, Santos AC, Francis SJ, Narayanan S, Brass SD, Arnold DL, Pike GB. Regional variations in normal brain shown by quantitative magnetization transfer imaging. *Magn. Reson. Med*. 2004; 51:299–303. [PubMed: 14755655]
- Smith SM. Fast robust automated brain extraction. *Hum. Brain Mapp*. 2002; 17:143–155. [PubMed: 12391568]
- Smith S, Golay X, Fatemi A, Mahmood A, Raymond G, Moser H, van Zijl P, Stanisz G. Quantitative magnetization transfer characteristics of the human cervical spinal cord in vivo: application to adrenomyeloneuropathy. *Magn. Reson. Med*. 2009; 61:22–27. [PubMed: 19097204]
- Stanisz G, Kecojevic A, Bronskill M, Henkelman R. Characterizing white matter with magnetization transfer and T_2 . *Magn. Reson. Med*. 1999; 42:1128–1136. [PubMed: 10571935]
- Underhill HR, Yuan C, Yarnykh VL. Direct quantitative comparison between cross-relaxation imaging and diffusion tensor imaging of the human brain at 3.0 T. *NeuroImage*. 2009; 47:1568–1578. [PubMed: 19500678]

- Underhill HR, Rostomily RC, Mikheev AM, Yuan C, Yarnykh VL. Fast bound pool fraction imaging of the in vivo rat brain: association with myelin content and validation in the C6 glioma model. *NeuroImage*. 2011; 54:2052–2065. [PubMed: 21029782]
- Viola P, Wells WM. Alignment by maximization of mutual information. *Int. J. Comput. Vis.* 1997; 24:137–154.
- Wolff SD, Balaban RS. Magnetization transfer contrast (MTC) and tissue water proton relaxation in vivo. *Magn. Reson. Med.* 1989; 10:135–144. [PubMed: 2547135]
- Wright PJ, Mouglin OE, Totman JJ, Peters AM, Brookes MJ, Coxon R, Morris PE, Clemence M, Francis ST, Bowtell RW, Gowland PA. Water proton T_1 measurements in brain tissue at 7, 3, and 1.5 T using IR-EPI, IR-TSE, and MPRAGE: results and optimization. *MAGMA*. 2008; 21:121–130. [PubMed: 18259791]
- Yarnykh VL. Actual flip-angle imaging in the pulsed steady state: a method for rapid three-dimensional mapping of the transmitted radiofrequency field. *Magn. Reson. Med.* 2007; 57:192–200. [PubMed: 17191242]
- Yarnykh VL, Yuan C. Cross-relaxation imaging reveals detailed anatomy of white matter fiber tracts in the human brain. *NeuroImage*. 2004; 23:409–424. [PubMed: 15325389]

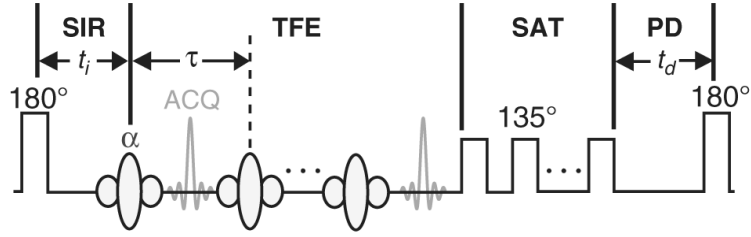
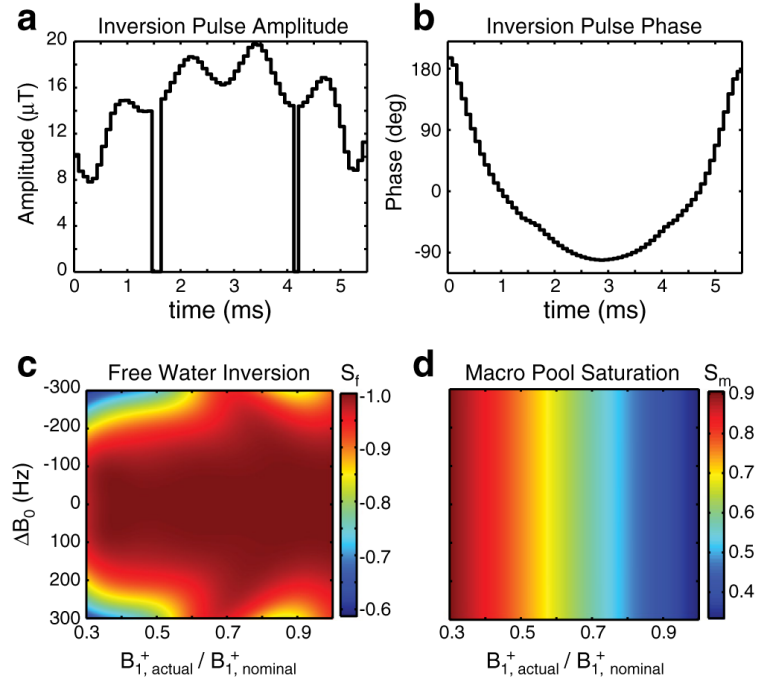


Fig. 1. SIR-TFE pulse sequence diagram. The sequence employs *i*) a composite inversion pulse (Fig. 2) designed to uniformly invert M_{zf} over a range of expected ΔB_0 and B_1^+ values with minimal macromolecular pool saturation, *ii*) a variable duration inversion recovery (SIR) period to sample the free pool recovery, *iii*) a TFE readout to efficiently cover k -space, *iv*) a pulse train to saturate (SAT) the free and macromolecular pools (allows $t_d < 5/\lambda^-$), and *v*) a pre-delay (PD) period to allow for partial M_z recovery. Legend: t_i = inversion time, t_d = pre-delay, τ = TFE pulse-to-pulse interval, ACQ = acquisition.

**Fig. 2.**

Composite inversion pulse amplitudes (a), phases (b), predicted free water inversion efficiency S_f (c), and predicted macromolecular saturation fractions S_m (d). $S_f = -1$ denotes complete inversion; $S_m = 1$ denotes no saturation. The two zero-amplitude discontinuities in the RF pulse (a) are a consequence of the power constraint used in the minimization procedure. The RF phase (b) of the pulse at these discontinuities is arbitrary; therefore, the phase at these points was set based upon linear interpolation of the neighboring RF phases for display purposes.

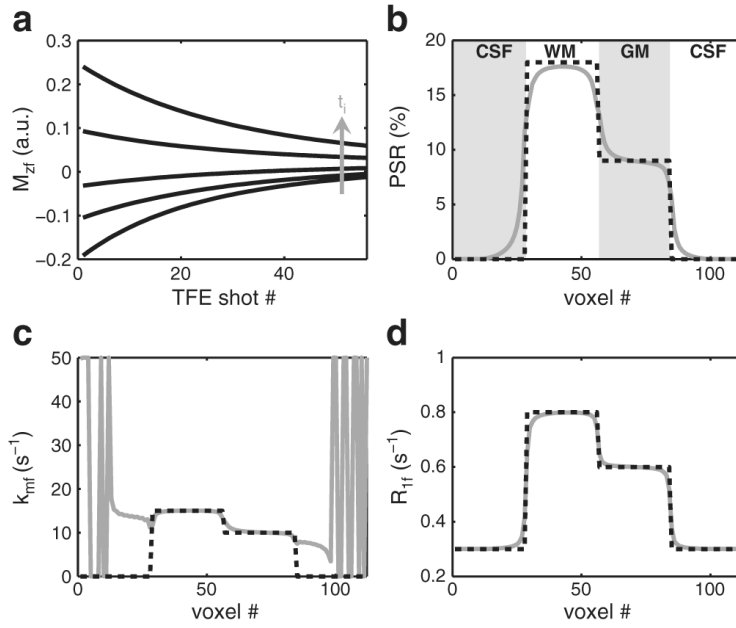


Fig. 3. Numerical simulations of the SIR-TFE readout (a) and resulting qMT parameter fits for the 1D test object defined in (b–d). (a) The M_{zf} for each region (WM shown here) and t_i was simulated and reordered into the corresponding k -space filter. The resulting filters were applied to the 1D test object as described in the text. (b–d) From the simulated fit parameters (solid gray lines), it can be seen that the TFE readout blurs the parameter maps with little or no bias (except for k_{mf} in CSF regions, which do not exhibit an MT effect).

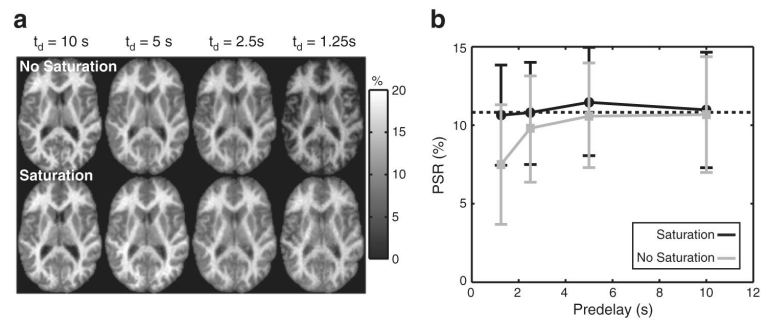


Fig. 4.

(a) Maps of PSR as a function of t_d without (top) and with (bottom) a post-TFE saturation train and (b) corresponding mean (\pm SD) slice-wise PSR values. For scans with the saturation train, all PSR values were nearly identical to the values at full recovery (dashed line). Without the saturation train, PSR values were increasingly underestimated with decreasing t_d .

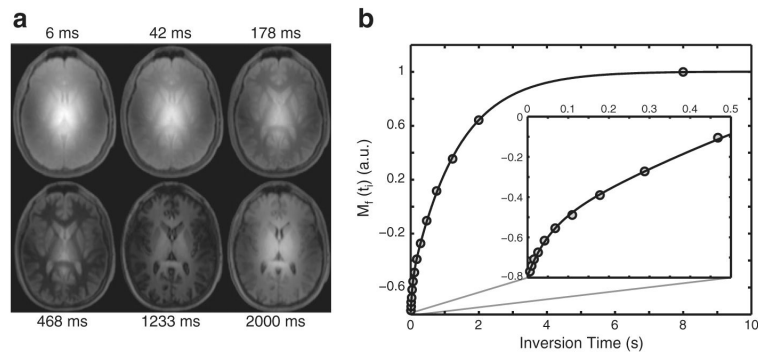


Fig. 5. Sample SIR-TFE images (a) and model fit (b) from a slice at the level of the lateral ventricles in a healthy control. (a) Images from six of the 14 inversion times are shown. Note the characteristic center brightening of the images due to B_1^+ inhomogeneities. (b) Corresponding SIR data from a voxel in the genu of the corpus callosum. Note the agreement between the SIR data (circles) and biexponential model [solid black line, Eq. (7)] and the deviation from a monoexponential model, which is apparent at the shortest inversion times shown in the zoomed inset.

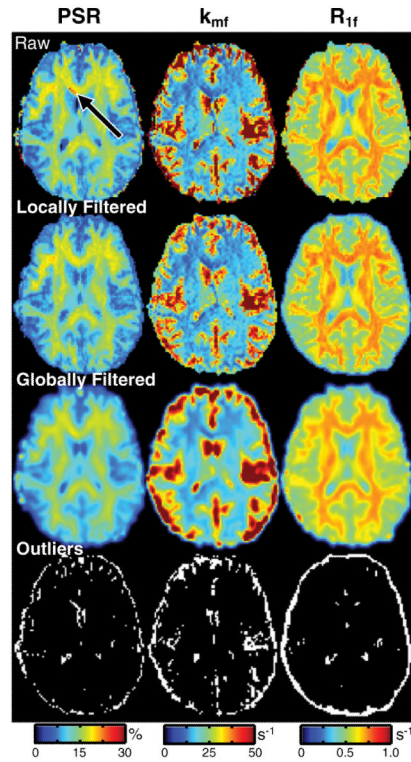


Fig. 6. Representative qMT parameter (PSR , k_{mf} , R_{1f}) maps with and without filtering. Shown are (1st row) raw parameter maps, (2nd row) parameter maps filtered with the locally-adaptive Gaussian filter, (3rd row) parameter maps filtered with the global Gaussian filter (with an identical kernel), and (4th row) masks of the outliers detected using the locally-adaptive filter. The arrow identifies a region with biased PSR values that are corrected by filtering. Note that the color-scale in these maps was chosen to highlight the outliers and is different than in Figs. 4 and 8.

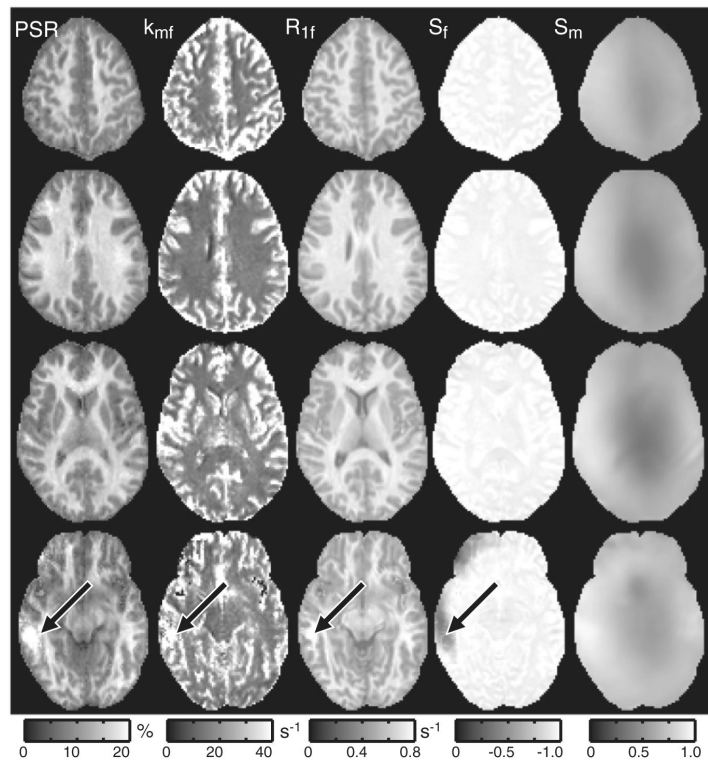


Fig. 7.

Representative parameter maps from one subject (four of 30 slices are shown). The qMT parameters (PSR , k_{mf} , R_{1f}) and the inversion efficiency S_f were uniform over most of the volume despite the presence of large field inhomogeneities. There does, however, appear to be some bias in the qMT parameter values in midbrain slices (black arrows), which typically exhibit the largest B_0 and B_1^+ inhomogeneities. This results in a deviation of S_f from -1 in these regions.

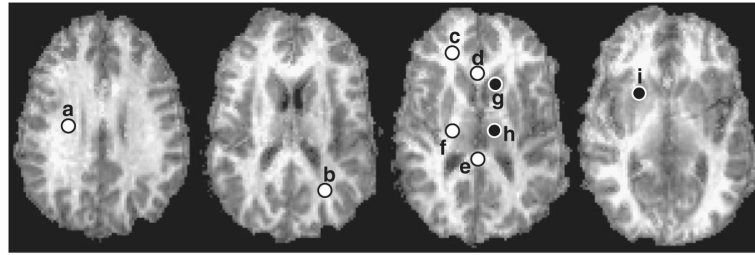


Fig. 8.

Representative *PSR* maps from a single volunteer with corresponding ROIs (*a*=corona radiata; *b*=occipital WM; *c*=frontal WM; *d*=corpus callosum, genu; *e*=corpus callosum, splenium; *f*=internal capsule; *g*=head of caudate; *h*=thalamus; *i*=putamen). White and black dots represent WM and GM ROIs, respectively. In practice, ROIs were defined bilaterally and results were averaged across hemispheres. Here we show ROIs in one hemisphere for display purposes.

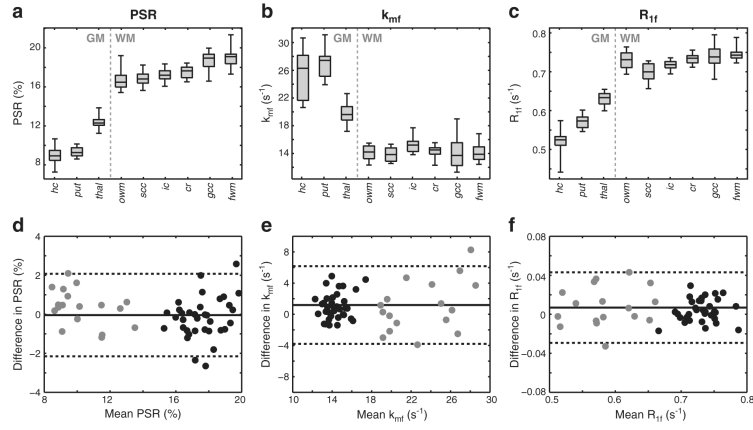


Fig. 9. (a–c) Boxplot of the mean ROI qMT parameters (*hc* = head of caudate; *put* = putamen; *thal* = thalamus; *owm* = occipital WM; *scc* = corpus callosum, splenium; *ic* = internal capsule; *cr* = corona radiata; *gcc* = corpus callosum, genu; *fwm* = frontal WM). On each box, the central mark is the median, the edges of the box are the 25th and 75th percentiles, and the whiskers extend to the most extreme data points. (d–f) Bland–Altman plots of the difference in parameters for WM (black) and GM (gray) ROIs across scans. The solid line is the mean difference, and the dashed lines are the limits of agreement (mean difference±1.96 SD).

Table 1

Test–retest reproducibility analysis of each qMT parameter (PSR, R_{1f} , and k_{mf}). Shown are the mean \pm SD parameter values across all ROIs for the test and retest scans, the resulting mean paired-difference between time-points, the limits-of-agreement (LOA), and the mean \pm SD test–retest coefficient of variation (CV_{retest}) across all ROIs. For comparison, the corresponding across-cohort coefficient of variation (CV_{cohort}) is also given.

Parameter	Test scan (mean \pm SD)	Retest scan (mean \pm SD)	Difference	LOA	CV _{retest} (%)	CV _{cohort} (%)
PSR (%)	15.2 \pm 3.9	15.2 \pm 3.7	0.0	(-2.2, 2.1)	4.9 \pm 1.5	5.6 \pm 1.9
k_{mf} (s ⁻¹)	16.8 \pm 4.7	18.0 \pm 5.5	1.2	(-3.9, 6.3)	8.2 \pm 2.4	9.4 \pm 3.6
R_{-1f} (s ⁻¹)	0.68 \pm 0.08	0.68 \pm 0.08	0.01	(-0.03, 0.04)	1.9 \pm 1.4	3.2 \pm 1.3